


A super-heterodyne passive 35 GHz millimeter-wave imaging system for detecting hidden objects

Hamideh Khosousi Sani¹, Shahram Mohanna¹  and Amir Nader Askarpour²

¹Communications Engineering Department, University of Sistan and Baluchestan, Zahedan 9816745785, Iran and ²Communications Engineering Department, Amirkabir University of Technology, Tehran 15875-4413, Iran

Research Paper

Cite this article: Khosousi Sani H, Mohanna S, Askarpour AN (2023). A super-heterodyne passive 35 GHz millimeter-wave imaging system for detecting hidden objects. *International Journal of Microwave and Wireless Technologies* **15**, 1483–1494. <https://doi.org/10.1017/S1759078723000405>

Received: 3 December 2022
Revised: 23 March 2023
Accepted: 27 March 2023

Keywords:

Passive millimeter-wave imaging system; SIW filter; spatial resolution

Corresponding author:

Shahram Mohanna,
E-mail: mohana@ece.usb.ac.ir

Abstract

Passive millimeter-wave imaging systems (PMWIS) are employed for detecting concealed objects by mapping millimeter waves emitted from materials or living tissues. The emitted waves are measured by a receiver or radiometers without employing external wave sources. In this paper, a new super-heterodyne receiver front-end of a PMWIS at 35 GHz with an even order band pass filter is simulated and implemented. The receiver has a suitable temperature resolution for the use of hidden object imaging, is integrated and lightweight assembled on one-layer board. It has a bandwidth of 1.5 GHz, a noise figure (NF) of 2.2, and a temperature resolution of 0.126 K. The even order filter is implemented based on the substrate-integrated waveguide (SIW) technology, with Chebyshev response. The filters are designed at the central frequency of 35 GHz with the bandwidth of 1.5 GHz and one of them has controllable transmission zeroes. The filters are made by printed circuit board technology, employing SIW as resonators, having a high-quality factor of 23.33. Additionally, a triple-stage radio frequency (RF) low noise amplifier has been implemented having the specification of: RF 34.25–35.75 GHz; bandwidth 1.5 GHz; gain >60 dB; NF <2.3 dB, which are better indexes compared to some other works.

Introduction

Passive millimeter-wave imaging systems (PMWIS) are of interest in medical diagnostics and security. In this context, passive means not deploying radiated waves on objects, while using the intrinsic millimeter-wave emissions from objects to reconstruct images [1]. In addition to reducing the risks of radiation on the body and objects, the un-traceability of the system is an advantage of the PMWIS for security applications. In some frequency bands, i.e. 35, 94, and 140 GHz, the attenuation rate of atmospheric absorption is lower than the nearby frequencies in the presence of air floating particles such as dust, smoke, and thick fog. Therefore, passive millimeter-wave receivers are a good candidate for various applications such as navigation [2]. Millimeter waves pass through the garment with low attenuation, so it is suitable to be employed in security [3] and medical imaging systems [4]. A millimeter wave's receiver (radiometer) detects noise-like emitted power received from an object taking into account the noise-equivalent temperature of the receiver. The output voltage of the radiometer is proportional to the noise power received from the objects' area. Typically, radiometers are designed with two types of structures for detection: direct detectors [5–7] and detectors with frequency converting (super-heterodyne) [8–10]. In direct detector systems, the radio frequency (RF) signal received from the antenna is transmitted directly to the detector diode after amplification by a low noise amplifier (LNA), employing a filter operating in the desired bandwidth and detector diodes with high response and low noise. Super-heterodyne detection has benefits in terms of design and manufacturing complexity as well as implementation costs. Figure 1 shows a block diagram of a heterodyne radiometer. The RF signal is received by the antenna, amplified by an LNA, then the frequency is converted to an intermediate frequency (IF), set by the local oscillator (LO) frequency. Different types of receivers can be designed for different applications, depending on the choice of LO frequency and IF bandwidth.

In this research, a 35 GHz super-heterodyne PMWIS is simulated and implemented. This paper describes two sections of the PMWIS; the design and fabrication of the super-heterodyne receiver structure and the RF filter. The ADS software is used to perform simulations and the analysis of the super-heterodyne receiver. Also, the HFSS software is employed to design the RF filter.

PMWIS specification

As shown in Fig. 1, the PMWIS super-heterodyne receiver includes an antenna, an LNA, an RF amplifier, an RF filter to reject out-band harmonics, a mixer with LO, an IF filter, an IF

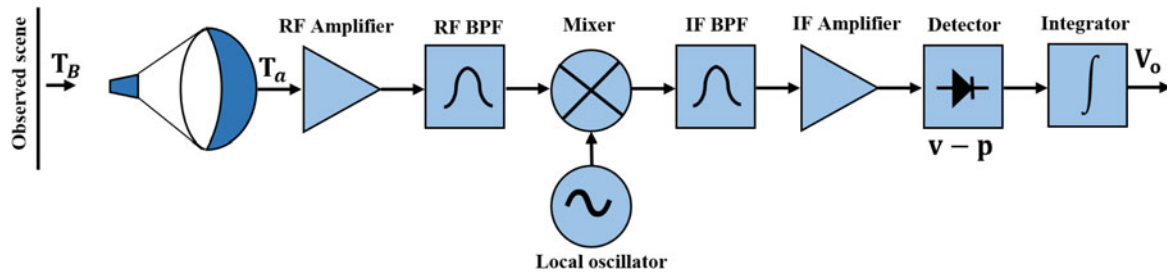


Figure 1. Configuration of a PMWIS super-heterodyne receiver [11].

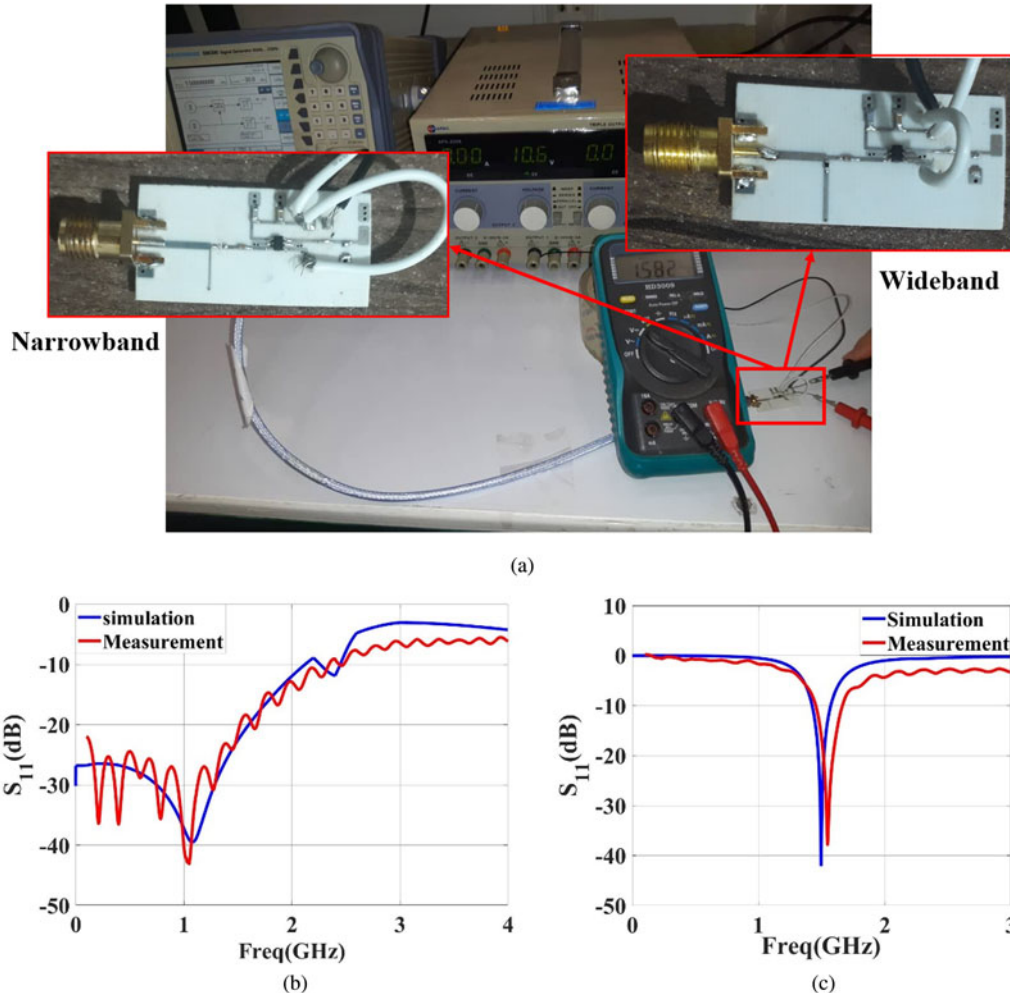


Figure 2. (a) Impedance matching circuit designed for the detector diode. (b) s_{11} diagram for a wide band. (c) s_{11} diagram for a narrow band.

amplifier, a detector diode, and an integrator. The output signal is sent to a video amplifier, an analog to digital converter, and to the computer to create an image [11].

The power received by the antenna is $P_a = k\Delta f T_a$, where Δf (Hz) is the bandwidth (equal to the IF bandwidth), $T_a(k)$ is the antenna temperature, and K is the Boltzmann constant (1.38×10^{-23} J/K). This is considered as the signal at the receiver input. The receiver equivalent noise power at the receiver input is $P_r = k\Delta f T_r$, where $T_r(k)$ is the receiver noise temperature (due to the thermal noise in the receiver components). In this case, the detector gives an analog output voltage proportional to the received noise power, which

can be calculated by equation (1) [12].

$$V_{out} = GK\Delta f(T_r + T_a) + V_{offset} \tag{1}$$

where, V_{offset} (V) is the detector offset voltage and G is the receiver gain. To reduce the system noise, the RF amplifier should have low noise and high gain for the detection of very small wave powers. The temperature resolution is defined as the lowest temperature difference which can be detected by the system or the temperature sensitivity of the system is obtained by equation (2) [13].

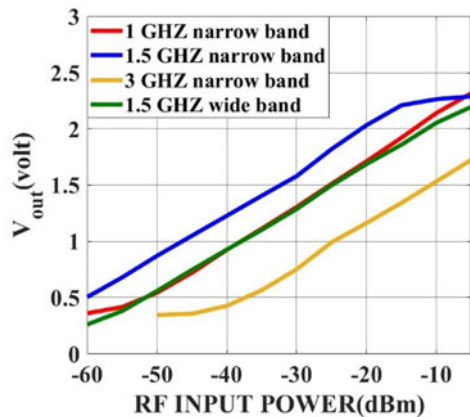


Figure 3. Detector output voltage and measured diagram in terms of input power.

$$\Delta T = (T_a + T_r) \sqrt{\frac{1}{\Delta f \tau} + \left(\frac{\Delta G}{G}\right)^2} \quad (2)$$

where, $\Delta G/G$ is the receiver gain fluctuations and $\tau(s)$ is the integration time of the low-pass filter after the detector. In order to improve the temperature resolution, the temperature equivalent to the system noise must be reduced and its integration time and bandwidth must be increased. It should be noted that a large increase in integration time will increase the imaging time but also increases the gain fluctuations. In the PMWIS, Δf is the IF bandwidth which in this receiver is 1.5 GHz. An acceptable threshold for ΔT is 0.5 K in most passive imaging systems [6, 14]. Therefore, using equation (2) and considering 10 ms for the integration time and ignoring the small gain fluctuations, the temperature resolution of 0.126 K is obtained. In the process of designing the PMWIS, the total gains of the RF and IF amplifiers and the responsivity of the diode should be considered to provide a

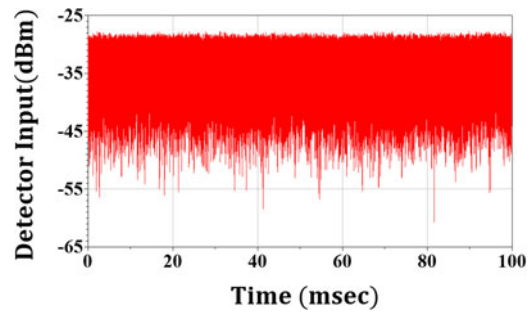


Figure 5. Received power to the diode for the temperature of 313 K.

suitable input power level required for detection. According to Rayleigh–Jeans law, the power level of the received signal for the bandwidth of 1.5 GHz at brightness temperature (T_B) of 273 k is -82.47 dBm, which is very small. Therefore, the RF amplifier must have high gain and low noise characteristics to provide the power level required for the diode detector.

Also, the loss in the IF amplifier, the mixer attenuators, and the filters must be considered. Since the central frequency is 35 GHz, a mixer with LO of 33.5 GHz is used to convert the signal to the IF of 1.5 GHz. Thus, the diode must have an appropriate sensitivity at the frequency of 1.5 GHz, so an RF power detector with a 60 dB dynamic range is employed (LT5534 (<https://www.analog.com/media/en/technical-documentation/data-sheets/5534fc.pdf>)). It operates in the range of 50 MHz to 3 GHz. Designing an input impedance matching network for the diode is challenging, the wider bandwidth the lower the detector sensitivity. Figure 2 (a) shows the matching circuit for the detector diode. Figures 2 (b) and 2(c) illustrate the S_{11} diagram representing the input impedance matching in both narrowband and wideband modes. Figure 3 indicates the output voltage (volts) of the detector versus the input power in both narrowband and wideband modes. As can be seen in Fig. 3, a suitable sensitivity for the imaging application has been obtained. Therefore, the components of the

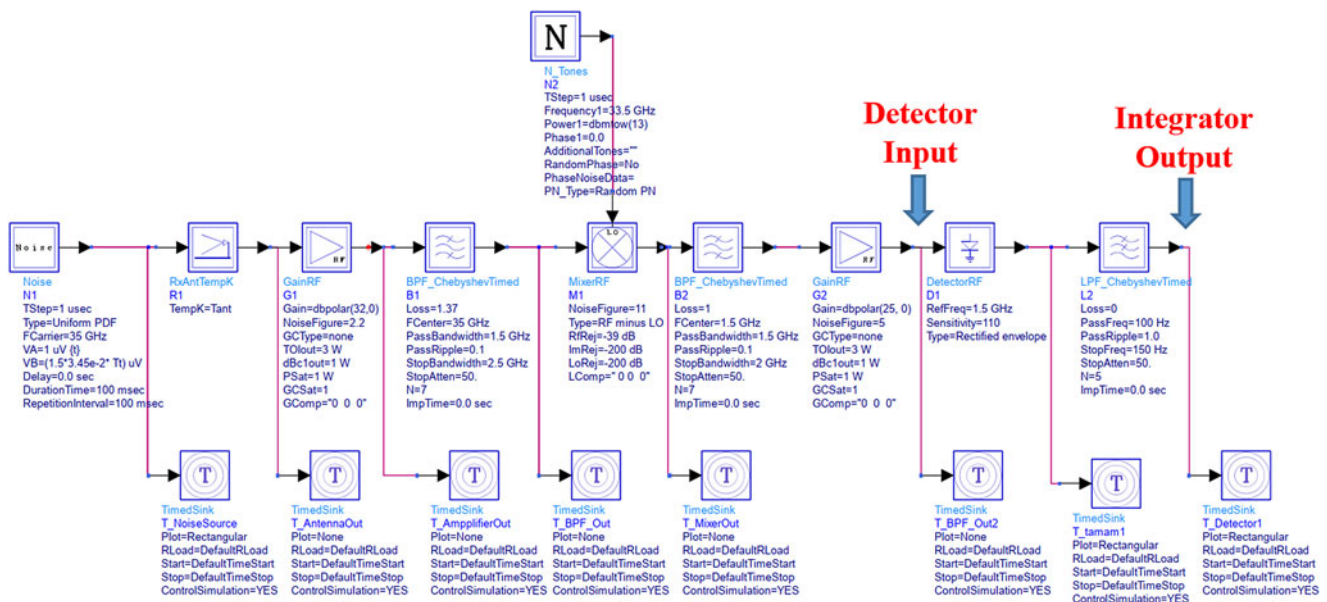


Figure 4. Super-heterodyne receiver.

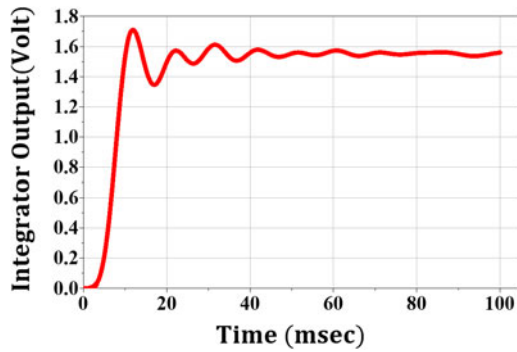


Figure 6. The output voltage of the system for a temperature of 313 K.

receiver, operating before the detector, must be designed in such a way that the necessary power is obtained.

Typically, commercial RF LNA components have a noise figure (NF) of 2.2 dB and a gain of 16 dB at 35 GHz. Therefore, two RF amplifiers are needed to provide the total gain of 32 dB. Additionally, two IF amplifiers with a total gain of 40 dB are utilized. The super-heterodyne receiver is simulated and shown in Fig. 4 and the received power that reached the detector is plotted in Fig. 5.

In the simulation, the attenuations of the mixer and the filter are considered. After the detector, an integrator (low-pass amplifier) is employed to eliminate high frequencies and smooth the output having 100 Hz bandwidth. In the image, the voltage difference between the pixels is equivalent to the temperature difference

between the regions. The output voltage is plotted in Fig. 6 for a temperature of 313 K. The output voltage is equivalent to the object temperature and includes some ripples in the time duration of the measurement (scanning the object).

The amplitude of these ripples depends on the bandwidth of the low-pass filter. To eliminate the ripples, it is necessary to calculate the mean of the voltage in the interval $\tau(s)$ for each pixel (scanned region) and map the voltage difference of regions in the scanned object as an image.

Filter design method

Microwave components in communication systems are required to be compact, and show high performance. To implement Ka-band filters with low insertion loss, low cost, and high power capacity, the substrate-integrated waveguide (SIW) [15] can entirely meet the above requirements, besides, the SIW circuit is fabricated by standard printed circuit board (PCB) process, which is very low weight and easy to integrate with planar circuits. Therefore, SIW technology is employed for designing the millimeter-wave filters of the PMWIS, resonator antenna [16], slot antenna for terahertz application [17], etc. As shown in Fig. 7, the waveguide structure can be made by a pair of arrays of metal short circuit rods that act as fences to trap the electromagnetic wave inside. The SIW structure only supports the propagation of TE_{m0} electric transverse modes, similar to the TE_{m0} mode in rectangular waveguides. The lack of TM modes is useful for the design of the band-pass filter because it can eliminate some unwanted out-of-band harmonics.

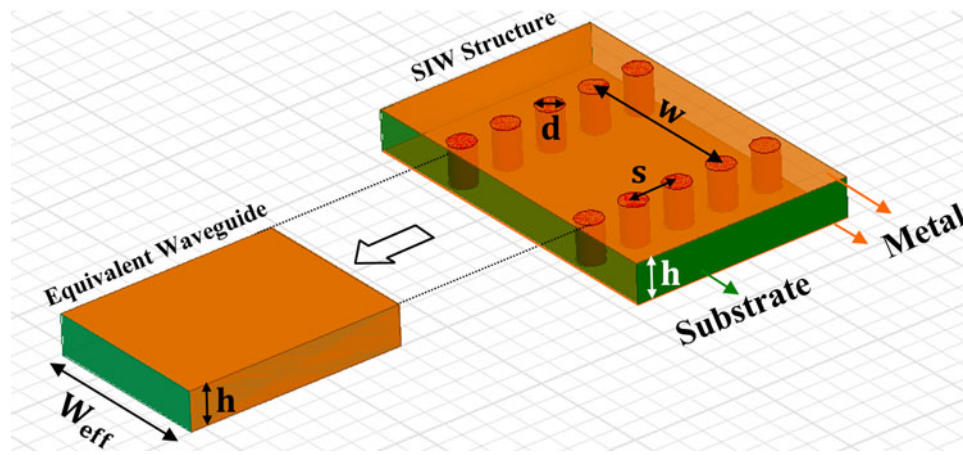


Figure 7. SIW structure and equivalent waveguide.

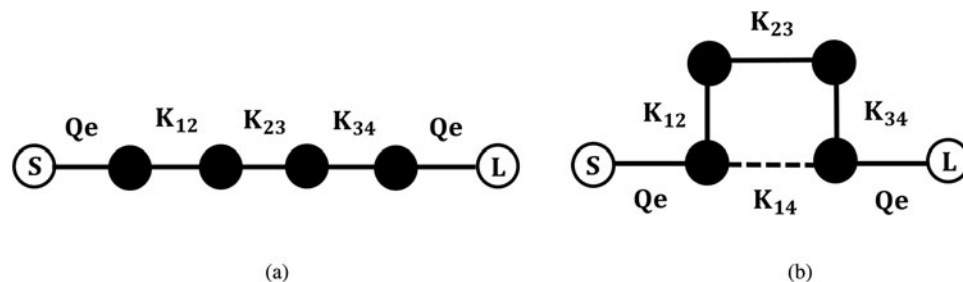


Figure 8. (a) Direct coupling and (b) quadruple structure filter with negative couplings (solid line: positive coupling, dashed line: negative coupling).

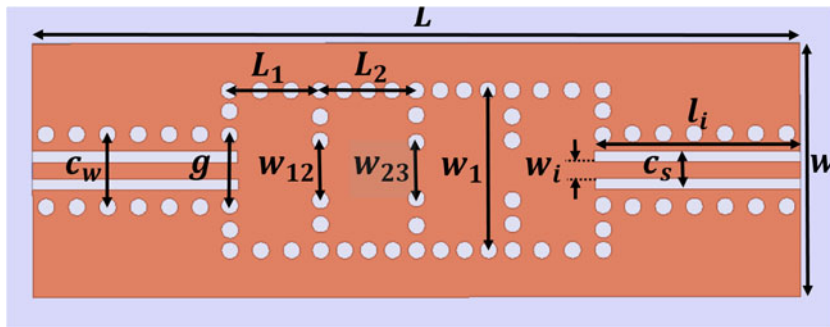


Figure 9. Designed filter structure.

Table 1. The filters dimensions

Parameter	Dimension (mm) Cascaded filter with direct coupling	Dimension (mm) Quadruple filter with direct coupling	Dimension (mm) Quadruple filter with cross-coupling	Parameter	Dimension (mm) Cascaded filter with direct coupling	Dimension (mm) Quadruple filter with direct coupling	Dimension (mm) Quadruple filter with cross-coupling
w	7.4	10.36	10.36	L_{io}	0.495	0.28	0.28
L	22.428	17.17	17.17	w_1	4.6575	2.72	2.715
l_i	6	6	6	L_1	2.649	4.56	4.56
g	2.0347	2.0347	2.0347	L_2	2.81	3.475	3.535
w_i	0.457	0.457	0.457	w_{12}	1.725	1.82	1.75
c_s	1.1176	1.1176	1.1176	w_{23}	1.615	1.32	1.37
c_w	2.11074	2.11074	2.11074	w_z	-	-	0.933
				L_z	-	-	3.855

The dimensions of an SIW must be determined to propagate a specific mode. The process of designing and determining SIW parameters is selecting s from the range of $0.05 < s/\lambda_c < 0.25$ and $0.5 < d/s < 0.8$ and then placing the parameters d and s in equation (3) and calculating w [18].

$$w = w_{eff} + s(0.766e^{0.4482d/s} - 1.176e^{-1.214d/s}) \quad (3)$$

At first, the even order Iris filter [19] with direct coupling as shown in Fig. 8(a), and SIW resonators are designed and simulated. Then based on direct coupling, one stage quadruple structure without negative coupling is designed just to obtain a relatively moderate attenuation slope in the stop band. The third-type filter is also realized as one stage quadruple structure, by

using a coplanar waveguide (CPW) line; to achieve negative coupling between cavity 1 and 4, it will generate two transmission zeroes (TZs) at each side of the pass band (Fig. 8(b)). Filters of cascaded quadruple structures generate pairs of TZs, the number of which depends on the order of the cascaded structure [20]. Therefore, adjusting different negative coupling coefficients in every block can obtain corresponding pairs of TZs in the stop band. This structure has one negative coupling and three positive couplings [21], the dotted line in Fig. 8(b) indicates negative coupling (electric field coupling), and the solid line indicates positive coupling (magnetic field coupling). Same structure filter with cross-couplings improves stop band performance with a steeper attenuation slope. In the negative cross-coupling filter, there exists one non-adjacent electric field coupling by CPW line and three adjacent magnetic field coupling by post-wall irises. CPW line is used to achieve negative coupling to obtain a single pair of TZs at each side of the pass band. Therefore, two controllable zeroes on both sides of the pass band are designed. Finally, a cascaded filter with direct coupling is used in the receiver. The filter is light weight and compatible with PCB manufacturing technology, due to the fact that they use SIW resonators.

Firstly, considering the insertion loss L_{Ar} (dB) = 0.1 dB and a minimum attenuation of stopband L_{As} (dB) at $\Omega = \Omega_s$ (Rad/s), the order of the low-pass Chebyshev prototype filter, with the mentioned characteristics, is obtained $n = 4$ from equation (4) [22]:

$$n \geq \frac{\cosh^{-1} \sqrt{(10^{0.1L_{As}} - 1/10^{0.1L_{Ar}} - 1)}}{\cosh^{-1} \Omega_s} \quad (4)$$

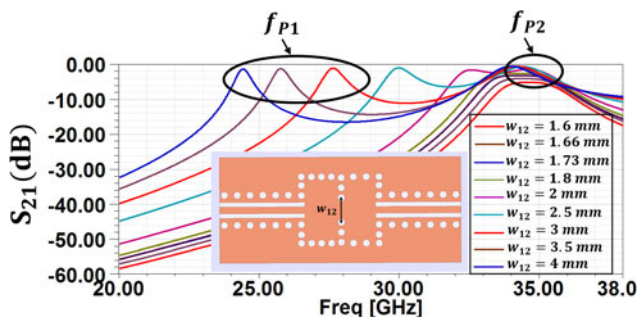


Figure 10. Diagram of extracting the k_{12} coupling coefficient in terms of w_{12} .

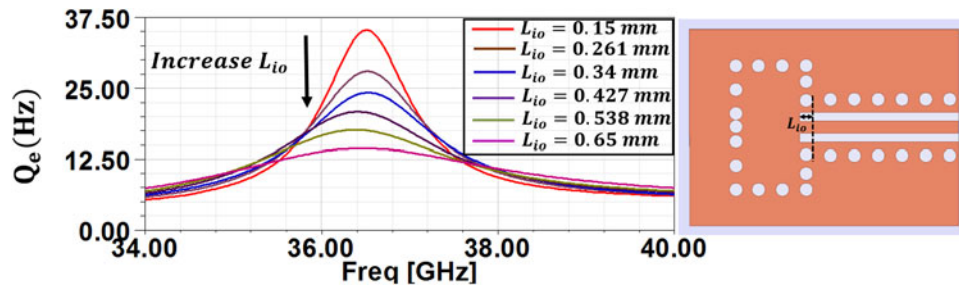


Figure 11. Simulated changes in external quality factor (Q_e) in terms of L_{io} .

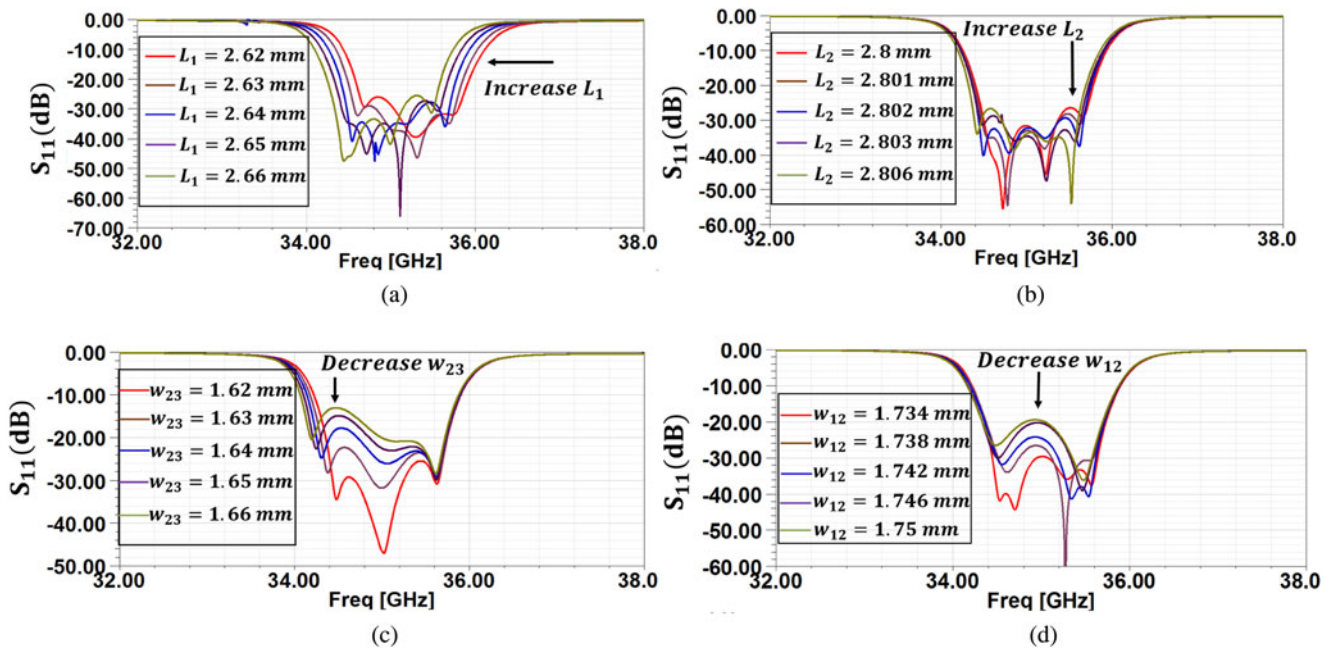


Figure 12. Simulated S_{11} of cascaded direct coupling filter versus the (a) L_1 , (b) L_2 , (c) w_{23} , (d) w_{12} .

Since the Iris method is used to design the filter, direct coupling relations must be used to calculate the coupling coefficients and the external quality factor. The fractional bandwidth (FBW) and the central angular frequency (ω_0) are calculated by the following relations [23]:

$$FBW = \frac{w_2 - w_1}{w_0} \tag{5}$$

$$\omega_0 = \sqrt{w_1 w_2} \tag{6}$$

Therefore, the presented external quality factor and the coupling coefficients are [22]:

$$Q_e = \frac{g_0 g_1}{FBW} \tag{7}$$

$$K_{i+1} = \frac{FBW}{\sqrt{g_i g_{i+1}}} \quad i = 1, 2, \dots, n - 1 \tag{8}$$

where n is the filter order and g_i s are the values of the low-pass prototype filter elements. After calculating the coupling coefficients required for the specified filter specifications, the next important step is to establish a relationship between each of the coupling coefficients with the physical structure of the coupled resonators, to determine the physical dimensions of the filter to be constructed. In order to calculate the coupling coefficient of tuned asynchronous resonators (i.e. the resonant frequency of each resonator is different), regardless of the coupling type, equation (9) is used [22]:

$$k = \pm \frac{1}{2} \left(\frac{f_{02}}{f_{01}} + \frac{f_{01}}{f_{02}} \right) \sqrt{\left(\frac{f_{p2}^2 - f_{p1}^2}{f_{p2}^2 + f_{p1}^2} \right)^2 - \left(\frac{f_{02}^2 - f_{01}^2}{f_{02}^2 + f_{01}^2} \right)^2} \tag{9}$$

where f_{0i} ($i = 1, 2$) represents the self-resonant frequency of each resonator without having any coupling with its neighboring counterpart and f_{pi} ($i = 1, 2$) denotes the two split resonant frequencies when two resonators are coupled to each other. If a particular coupling is considered a positive coupling, then a negative coupling refers to a coupling whose phase response is opposite to the positive coupling phase response. The phase response of a

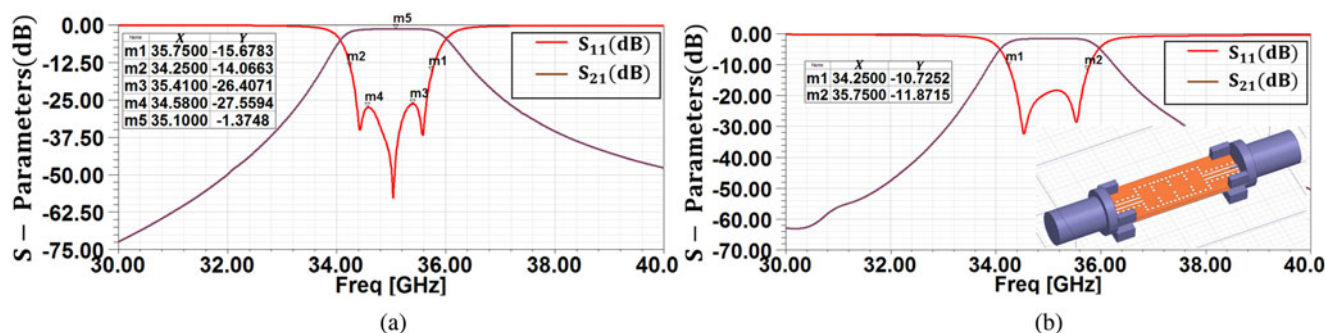


Figure 13. Final filter output after optimization (a) without connector and (b) with connector.

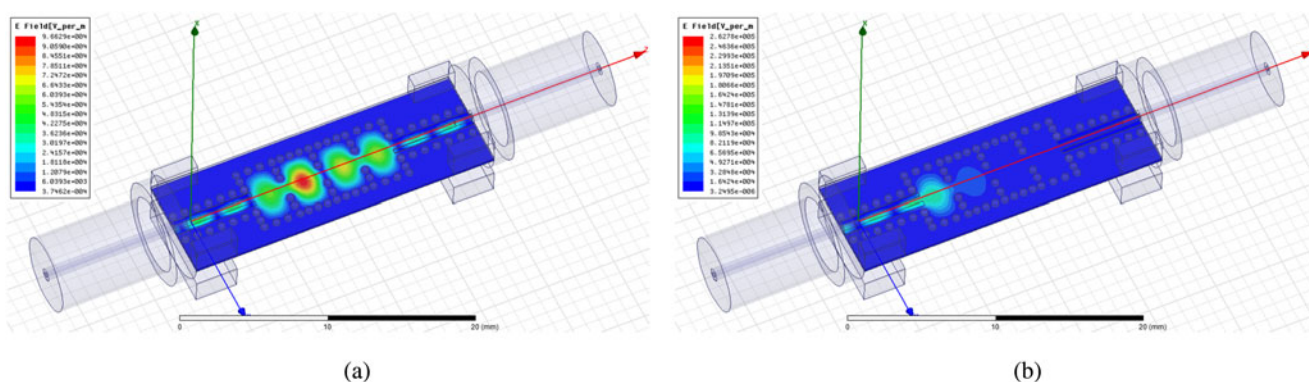


Figure 14. Electric field distribution for the (a) resonant frequency of cascaded filter with direct coupling at 35 GHz and (b) far away from the resonant mode at 33 GHz.

coupling coefficient can be found from the S parameters of the coupling structure. To obtain the external quality factor of a resonator, the resonator can be excited by employing a feed line, so that there is no aperture as a load in it. The state, which is equivalent to a single-aperture network, is called a singly loaded resonator. In this case, the external quality factor is equal to [24]:

$$Q_e = \frac{w_0 \cdot \tau_{S_{11}}(w_0)}{4} \tag{10}$$

where w_0 is the resonant angular frequency and $\tau_{S_{11}}(w_0)$ is the group delay in the resonant frequency. To calculate the group delay, equation (11) is used, in which $\angle S_{11}$ is the phase of S_{11} .

$$\tau_{S_{11}}(w_0) = - \left. \frac{\partial(\angle S_{11})}{\partial w} \right|_{f=f_0} = - \frac{1}{2\pi} \left. \frac{\partial(\angle S_{11})}{\partial f} \right|_{f=f_0} \tag{11}$$

Designing the RF filter for PMWIS at 35 GHz central frequency

Having the bandwidth of 1.5 GHz and the central frequency of 35 GHz, the lower and upper cut-off frequencies of the BPF became $f_1 = 34.25$ GHz and $f_2 = 35.75$ GHz, respectively. By determining the characteristics of the desired filter, the values of the elements of the fourth-degree low-pass prototype filter are calculated. It is necessary to calculate the external quality factor Q_e and the coupling coefficients K . By placing g_i and $FBW = 0.042867$ in equations (7) and (8), these coefficients will be $Q_e = 24.214$, $k_{12} =$

$k_{34} = 0.037$ and $k_{23} = 0.029$. Using the SIW technology on the 8 mil Rogers 4003 substrate, the physical dimensions of the filter are obtained by simulation and optimization. Firstly, by placing the substrate specifications in the *LineCalc* tool of ADS software, the specifications of the grounded coplanar waveguide (GCPW) feed line that has an impedance of 50 ohms are determined, and w , C , s , l parameters. Then, using the methodology described in section “Designing the RF filter for PMWIS at 35 GHz central frequency,” the diameter of the vias and their distances are calculated. The diameter of the short-circuit rods $d_{via} = 0.5$ mm and the distance between them is maximally considered as $s = 0.9$ mm. However, reducing the distance of the vias reduces the physical strength of the filter. Figure 9 and Table 1 show the filter structure and its dimensional parameters.

The next step is to determine the dimensions of the resonators. The highest filter resonant frequency is 35.75 GHz. By placing the resonant frequency in equation (12), the dimensions of the waveguide resonating at this frequency are obtained $w_{eff} = \lambda = 4.4575$ mm and $L_{eff} = 2.5735$ mm. To obtain the equivalent SIW dimensions, equation (3) should be used, in which case $w = 4.82788$ mm and $L = 2.78738$ mm are calculated, and after optimization, $w_1 = 4.6575$ mm and $L_1 = 2.649$ mm [24]:

$$f_{TE101} = \frac{c}{2\sqrt{\mu_r \epsilon_r}} \sqrt{\left(\frac{1}{w_{eff}}\right)^2 + \left(\frac{1}{L_{eff}}\right)^2} \tag{12}$$

The method of obtaining the optimal values:

The resonant dimensions of 1 and 2 are the same as 3 with 4, respectively, due to the symmetry in this filter. The coupling

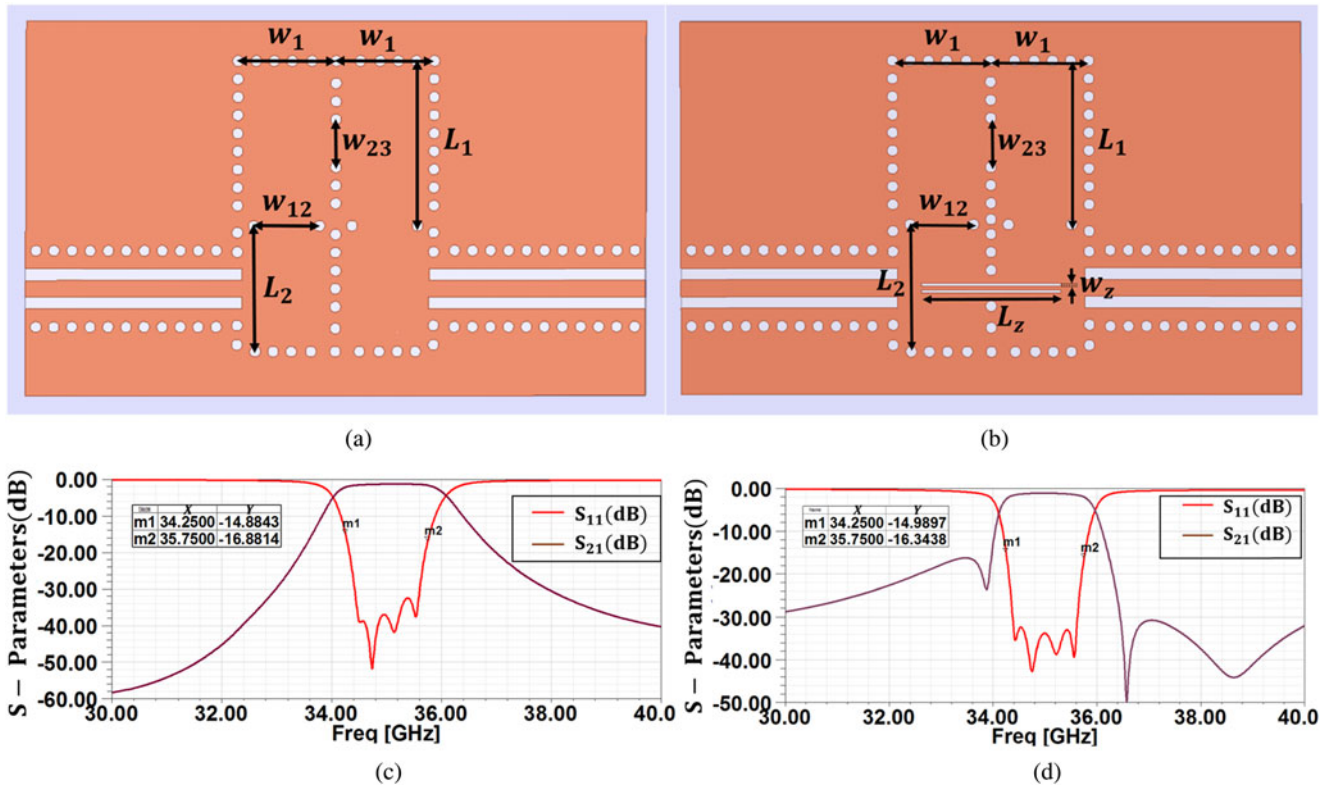


Figure 15. (a) Structure of quadruple filter with direct coupling. (b) Structure of quadruple filter with cross-coupling. (c) Simulation results of quadruple filter with direct coupling. (d) Simulation results of quadruple filter with cross-coupling.

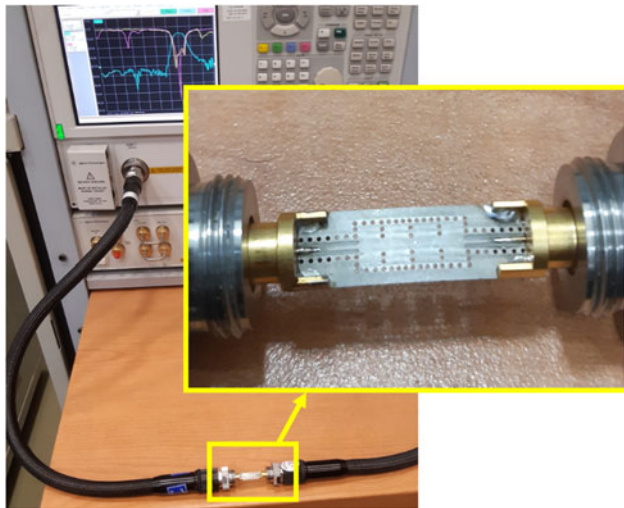


Figure 16. fabricated cascaded filter with direct coupling and test setup.

coefficients k_{12} , k_{23} , and k_{34} must be calculated in terms of distances w_{12} , w_{23} , and w_{34} , respectively, so $k_{12} = k_{34}$ and $w_{12} = w_{34}$. The coupling coefficients k_{12} and k_{23} are sufficient for the design due to the symmetry structure of the filter. To obtain k_{12} , the structure of Fig. 10 in HFSS software is swept parametrically versus changing w_{12} parameter. The result of the parametric sweep creates several scattering parameter curves $|s_{21}|$, which are shown in Fig. 10. By extracting the frequencies f_{p1} and f_{p2} from these curves, and using equation (9), k_{12} can be obtained in

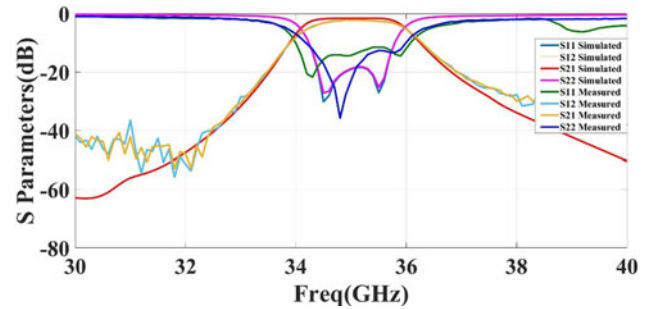


Figure 17. Comparison of measured and simulated results of cascaded filter with direct coupling.

terms of w_{12} . Since the dimensions of resonator 1 are not the same as the dimensions of resonator 2, so the self-frequencies of each resonator are not equal. By calculating the approximate values of the dimensions and optimization method, the precise dimensions can be computed. It can be assumed that the second resonator resonates at the same frequency as the first resonator, thus the values f_{01} and f_{02} can be considered equal to calculate k_{12} in equation (9). From the curves for $k_{12} = 0.03711$, the distance w_{12} is 1.73 mm. Performing a similar process, the changes in k_{23} can be obtained in terms of the distance w_{23} . According to simulations similar to w_{12} , for $k_{23} = 0.029$ the distance of w_{23} is 1.615 mm.

After that, the external quality factor (Q_e) must be calculated. To observe variations, Q_e of the structure in Fig. 11 must be parametrically swept in terms of L_{i0} . At each step of the parametric sweep, the group delay around the resonant frequency is obtained

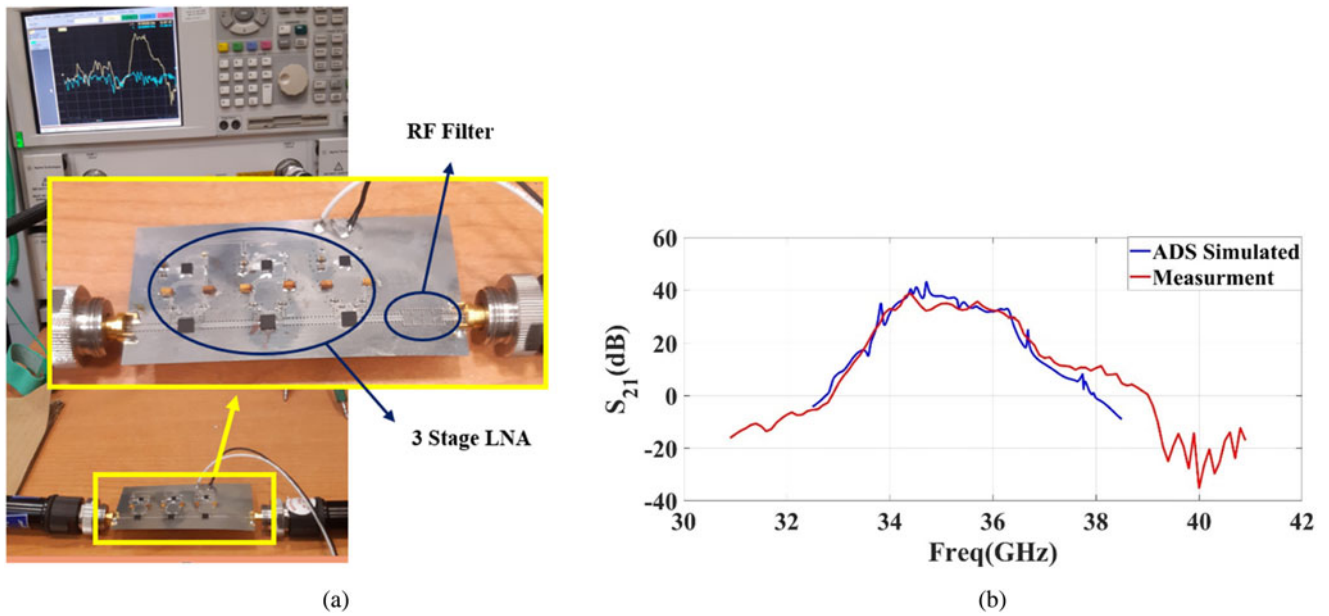


Figure 18. (a) fabricated filter integrated with amplifiers. (b) Gain.

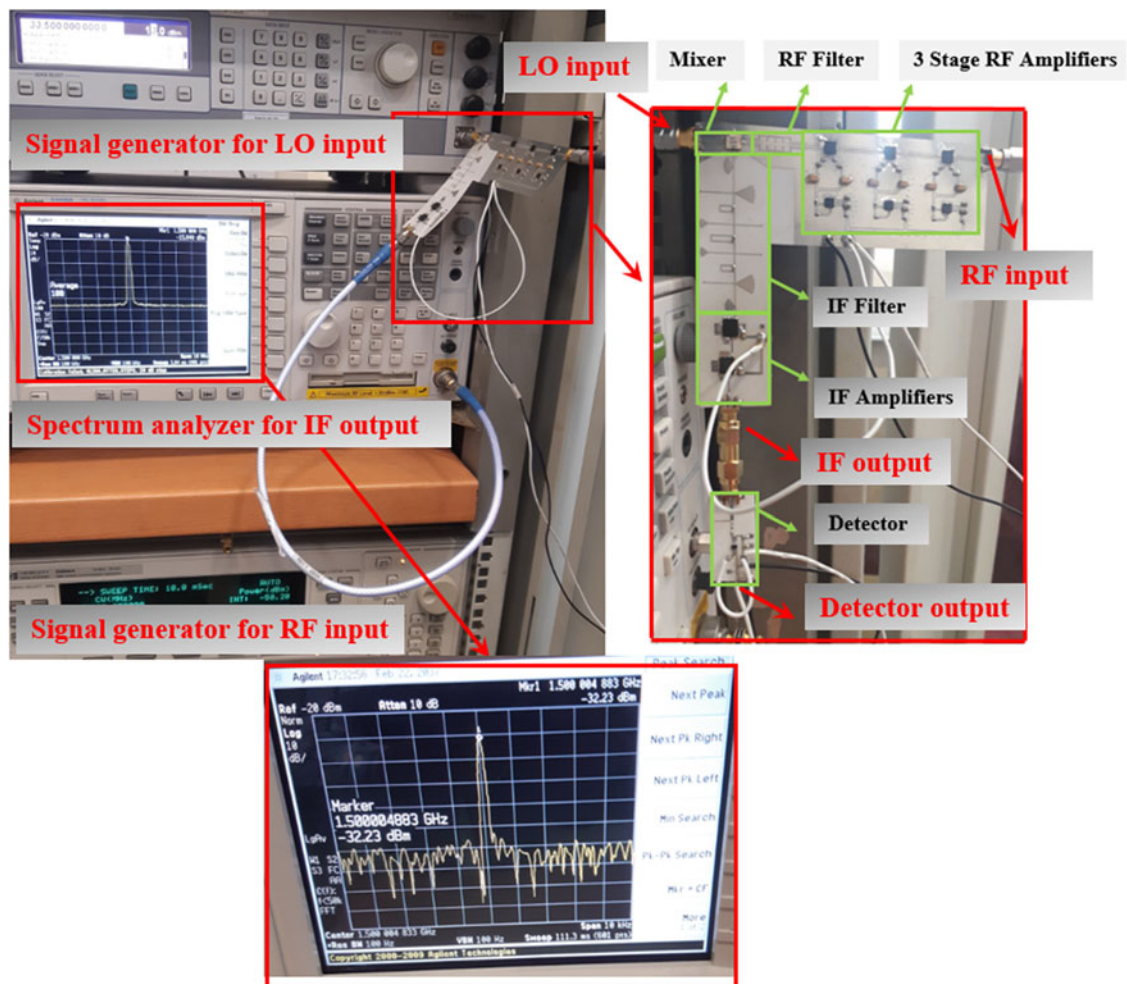


Figure 19. Experimental setup used for the determination of the final board bandwidth and available power gain.

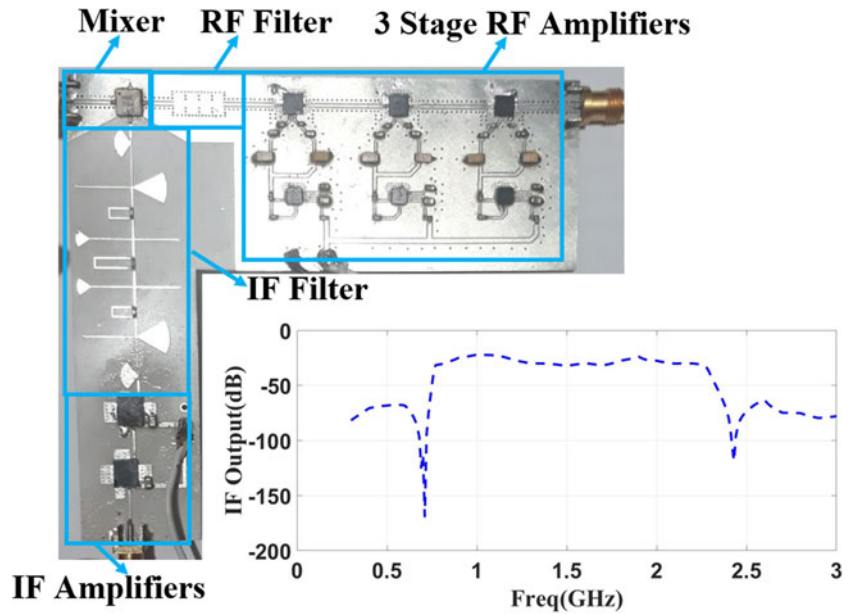


Figure 20. IF output.

Table 2. Comparison of different works with this project

Reference	RF frequency (GHz)	IF frequency (GHz)	LO frequency (GHz)	Noise figure (NF)(dB)	Gain (dB)	Band width (GHz)	Integration time (ms)	BPF
[25]	32 – 36	3.5 – 7.5	4 × 9.875	<4.5	33 ± 7.5	1	40	1 – type
[26]	34	2	8 × 4	4	40	0.3	–	1 – type
[27]	27.5 – 30.0	3.7	11.90 × 2 to 13.15 × 2	2.8	80	2	–	1 – type
[28]	94	1 – 18	3 × 31.5	–	–	18	3.33	None
	183	1 – 12	3 × 30.5	–	–	12	–	None
[29]	34.5 – 35.5	0.1	34.5 – 35.5	<8	<27	–	–	None
This project	34.25 – 35.75	0.75 – 2.25	33.5	<2.3	>60	1.5	10	3 – planar type

by placing the phase of S_{11} in equation (10). Q_e can then be calculated for different L_{io} using equation (11). Figure 11 shows the changes in Q_e with respect to L_{io} . According to Fig. 11, the length of L_{io} for $Q_e = 24.21$ is about 0.34 mm. After optimization of the parameters $L_{io} = 0.495$.

As mentioned above, it was assumed that the dimensions of the resonators are the same in the calculation of k_{12} and k_{23} , but in the following, the optimization method and accurate calculation of the parameters are described by studying the factors affecting the filter output. The filter specifications can be directed to the desired specifications by setting the four parameters L_1 , L_2 , w_{12} , and w_{23} . According to Fig. 12, L_1 affects the upper cut-off frequency. Therefore, after approximately calculating L_1 , the optimal value of L_1 can be calculated by partially changing L_1 , as shown in Fig. 12, so that the upper cut-off frequency is 35.75 GHz. Due to the coupling effects in the filter, each parameter has a significant effect on a specific part of the response (according to Fig. 10), and the exact value of each parameter can be determined.

After obtaining the dimensions of the filter and optimization, a complete simulation of the filter is performed and the filter output

is obtained as shown in Fig. 13(a). More accurately, the connectors also affect the outputs of the filter, so in order to test the filter with the connectors, the dimensions must be optimized with the presence of the connectors. As can be seen in Fig. 13(b), the responses are affected by the presence of the connectors.

The E -field distribution of the optimized structure is shown in Fig. 14 at different frequency. Figure 14(a) shows the distribution of E -field in the pass-band (at 35 GHz). According to Fig. 14(a) the input power transmitted to output port. Figure 14(b) shows the distribution of the E -field out of band (at 33 GHz), that is given the input power is not transmitted to output port.

Next, the square filter and the filter with mutual coupling are simulated and optimized. The diameter of the short-circuit rods $d_{via} = 0.3$ mm and the distance between them is maximally considered as $s = 0.5$ mm. The structure and simulation results of square filters with direct and cross-coupling are shown in Fig. 15. To verify the simulation results, the first filter was built and tested. The filter is implemented on an RO 4003 PCB as shown in Fig. 16.

The comparison of measured and simulated results is shown in Fig. 17, which indicates the results are almost equal. The use of connectors has altered the measurement results. Moreover, the existing manufacturing technology, which uses a thickness of 35 microns of copper, has caused more losses in the measurement results.

Fabrication of the LNA and the filter

In section "PMWIS specification" a two-stage LNA has been designed, as described in Fig. 4. Taking into account the losses of the connectors and transmission lines as well as some inaccuracies during the construction and soldering, it was estimated that the total gain may be decreased. Therefore, a new LNA employing three amplifiers has been designed and implemented as shown in Fig. 18(a). The simulation and measurement results of the amplifiers along with the filter are shown in Fig. 18(b). According to the datasheet, the input power to the amplifier must be -5 dBm as maximum. Thus, the input power of LNA must be small enough so that, after amplification by the initial two-stage amplifiers, the power transmitted to the third amplifier be less than -5 dBm. Figure 18(b) presents the result of combining amplifiers with the filter as a plot of S_{21} .

In order to have a light weight, small, and low-cost system with appropriate spatial resolution and temperature, all parts must be assembled on one board. All parts have been implemented with GCPW impedance matching lines in the RF part and microstrip lines in the IF part. Also, in order to be able to measure without the presence of the target and the temperature setup and by the signal generator, the entire components before the detector are placed on one single board and the detector part is placed on a separate board. To test the hot object, the antenna and the detector board must be connected to the main board. The antenna [11] and the detector were implemented in such a way that they can be re-integrated with the main board after the initial test. Figure 19 shows the measurement setup and the system under test.

To test the system of the super-heterodyne receiver front-end of the PMWIS, a signal with a frequency of 35 GHz and a power of -75 dBm is applied to the input part of the board, i.e. RF input, and a signal with a frequency of 33.5 GHz and a power of 13 dBm is applied to the LO of the mixer, i.e. LO input. It should be noted that the loss of the cable is also taken into account here, and due to the 5 dB attenuation of the cable, the power reaches to -80 dBm at the RF input point. In the LO input, the board is directly connected to the signal generator to avoid the cable loss. The bias voltage of the RF and IF amplifiers is 5 volts, which is supplied by the power supply. The IF output point is connected to the network analyzer to measure the power in terms of frequency. The results of IF output in the frequency range of 30–40 GHz considering -80 dBm power input are shown in Fig. 20. Additionally, in Table 2, a comparison has been made between the parameters achieved in this project and some other works.

The triple-stage RF LNA has been implemented having the specification of: RF 34.25–35.75 GHz; bandwidth 1.5 GHz; gain >60 dB; NF <2.3 dB. It has less overall integration time compared to some other works, referenced in Table 2. As a result, the target imaging time is decreased, where by reducing the NF, a suitable temperature resolution can be achieved. By using suitable filters at the RF and IF stages, a bandwidth of 1.5 GHz has been

obtained, which is wider than the referenced systems operated at the frequency range.

Conclusion

In this paper, a Ka-band super-heterodyne receiver front-end of a PMWIS at 35 GHz with a suitable band pass filter is simulated and implemented. Also an SIW even order filter with Chebyshev response suitable for the intended application is designed so that one of them has controllable TZs. The filters are designed at the same center frequency of 35 GHz with the same bandwidth of 1.5 GHz. Filters are made by PCB technology employing SIWs as resonators having a high-quality factor of 23.33. The receiver with RF filter has a suitable temperature resolution for the use of hidden object imaging, which is made as an integrated and lightweight one-layer board; and it has a bandwidth of 1.5 GHz, an NF of 2.2, and a temperature resolution of 0.126 K. Moreover, all components of this receiver are integrated in a single-layer PCB.

Acknowledgements. The authors thank Professor Abdolali Abdipour, Director of Microwave/MM-wave Research Lab at Amirkabir University of Technology, for providing the opportunity to perform the required tests in the lab.

Financial support. This research received no specific grant from any funding agency, commercial, or not-for-profit sectors.

Conflict of interest. None.

References

1. Nanzer JA (2012) *Microwave and Millimeter-Wave Remote Sensing for Security Applications*. Norwood, MA, USA: Artech House.
2. Fetterman MR, Grata J, Jubic G, Kiser WL Jr. and Visnansky A (2008) Simulation, acquisition and analysis of passive millimeter-wave images in remote sensing applications. *Optics Express* **16**, 20503–20515.
3. Appleby R and Anderton RN (2007) Millimeter-wave and submillimeter-wave imaging for security and surveillance. *Proceedings of the IEEE* **95**, 1683–1690.
4. Council NR (2007) *Assessment of Millimeter-Wave and Terahertz Technology for Detection and Identification of Concealed Explosives and Weapons*. Washington, DC, USA: National Academies Press.
5. Gilreath L, Jain V and Heydari P (2011) Design and analysis of a W-band SiGe direct-detection-based passive imaging receiver. *IEEE Journal of Solid-State Circuits* **46**, 2240–2252.
6. Lynch JJ, Moyer H, Schaffner J, Royter Y, Sokolich M, Hughes B, Yoon Y and Schulman J (2008) Passive millimeter-wave imaging module with preamplified zero-bias detection. *IEEE Transactions on Microwave Theory and Techniques* **56**, 1592–1600.
7. Tomkins A, Garcia P and Voinigescu SP (2010) A passive W-band imaging receiver in 65-nm bulk CMOS. *IEEE Journal of Solid-State Circuits* **45**, 1981–1991.
8. Li J and Zhang J (1999) Two new types of microwave radiometer: a computer gain compensative design and a real-time calibrated design. *Journal of Electronics* **16**, 277–283.
9. Zhou L, Wang C-C, Chen Z and Heydari P (2011) A W-band CMOS receiver chipset for millimeter-wave radiometer systems. *IEEE Journal of Solid-State Circuits* **46**, 378–391.
10. Kim Y-H, Kim S-H, Kang G-S, Kim H-S and Yang K-S (1999) 92 GHz radiometer system for remote sensing applications. In *Proceedings of the KSRS Conference*, pp. 462–467.
11. Sani HK, Mohanna S and Askarpour AN (2021) Implementing a passive millimeter wave imaging system (PMWIS) and its antenna for hidden object detection at frequency of 35 GHz. *Iranian Journal of Marine Technology* **8**, 1–12.

12. **Le Vine D and Skou N** (2006) *Microwave Radiometer Systems: Design and Analysis*. Norwood, MA, USA: Artech House.
13. **Tiuri ME** (1964) Radio astronomy receivers. *IEEE Transactions on Military Electronics* **8**, 264–272.
14. **Martin CA, González CEG, Kolinko VG and Lovberg JA** (2008) Rapid passive MMW security screening portal. In *Passive Millimeter-Wave Imaging Technology XI*, vol. 6948, pp. 117–125.
15. **Xu F and Wu K** (2005) Guided-wave and leakage characteristics of substrate integrated waveguide. *IEEE Transactions on Microwave Theory and Techniques* **53**, 66–73.
16. **Chemweno EK, Kumar P and Afullo TJO** (2023) Design of high-gain wideband substrate integrated waveguide dielectric resonator antenna for D-band applications. *Optik* **272**, 170261.
17. **Ur Rehman Kazim J, Abohmra A, Ur Rehman M, Imran MA and Abbasi QH** (2020) A corrugated SIW based slot antenna for terahertz application. *2020 IEEE International Symposium on Antennas and Propagation and North American Radio Science Meeting, Montreal, QC, Canada*, pp. 1407–1408.
18. **Kordiboroujeni Z and Bornemann J** (2013) Designing the width of substrate integrated waveguide structures. *IEEE Microwave and Wireless Components Letters* **23**, 518–520.
19. **Wang K, Wong S-W, Sun G-H, Chen ZN, Zhu L and Chu Q-X** (2015) Synthesis method for substrate-integrated waveguide bandpass filter with even-order Chebyshev response. *IEEE Transactions on Components, Packaging and Manufacturing Technology* **6**, 126–135.
20. **Levy R** (1995) Direct synthesis of cascaded quadruplet (CQ) filters. *IEEE Transactions on Microwave Theory and Techniques* **43**, 2940–2945.
21. **You CJ, Chen ZN, Zhu XW and Gong K** (2012) Single-layered SIW post-loaded electric coupling-enhanced structure and its filter applications. *IEEE Transactions on Microwave Theory and Techniques* **61**, 125–130.
22. **Hong J-SG and Lancaster MJ** (2004) *Microstrip Filters for RF/Microwave Applications*. New York, NY, USA: John Wiley & Sons.
23. **Matthaei G** (1980) *Microwave Filters, Impedance-Matching Networks and Coupling Structures*. Norwood, MA, USA: Artech House. pp. 775–809.
24. **Pozar DM** (2011) *Microwave Engineering*. New York, NY, USA: John Wiley & Sons.
25. **Chen X, Ye X, Wang C, Hu A and Miao J** (2018) A Ka band multi-channel integrated receiver for passive millimeter wave imaging system. In *2018 Progress in Electromagnetics Research Symposium (PIERS-Toyama)*, pp. 2099–2105.
26. **Mehdi G, Anyong H, Fu Y, Tongfei Y, Miao J and Khan ZB** (2013) A modular Ka-band front-end receiver for passive imaging system. In *INMIC*, pp. 121–124.
27. **Alimenti F, Mezzanotte P, Simoncini G, Palazzi V, Salvati R, Cicioni G, Roselli L, Dogo F, Pauletto S, Fragiaco M and Gregorio A** (2020) A Ka-band receiver front-end with noise injection calibration circuit for CubeSats inter-satellite links. *IEEE Access* **8**, 106785–106798.
28. **Viegas C, Alderman B, Powell J, Liu H, Wang H and Sloan R** (2015) Millimeter wave radiometers for applications in imaging and nondestructive testing. In *2015 8th UK, Europe, China Millimeter Waves and THz Technology Workshop (UCMMT)*, pp. 1–4.
29. **Xia L, Xu R and Yan B** (2006) LTCC-based highly integrated millimeter-wave receiver front-end module. *International Journal of Infrared and Millimeter Waves* **27**, 975–983.



2008. Her expertise is microwave/mm-wave and systems.



then moved to the University of Sistan and Baluchestan as an associate professor. As a multidisciplinary researcher, skillful in microwave imaging, electromagnetic tomography, ultrasonic and wireless sensors, and related physics and mathematics, he has contributed to the discipline by delivering 18 articles in international conferences and publishing 27 papers in indexed journals.



Dr. Amir Nader Askarpour received the B.S. degree in electrical engineering from the Sharif University of Technology, Tehran, Iran, in 2004, and the M.S. and Ph.D. degrees in electrical engineering from the University of Tehran, Tehran, in 2006 and 2012, respectively. He was a post-doctoral researcher with the University of Texas, Austin, TX, USA, from 2012 to 2014. He is currently an assistant professor with the Amirkabir University of Technology (Tehran Polytechnic), Tehran, and also a member of the Microwave/MM-Wave and Wireless Communication Research Laboratory. He delivered several articles in international conferences and has published 17 papers in indexed journals.

Hamideh Khosousi Sani is currently a doctoral student in the Faculty of Electrical and Computer Engineering at the University of Sistan and Baluchestan. She received an M.Sc. degree in the field of electrical and telecommunication engineering from Imam Khomeini International University of Qazvin in 2011 and a B.Sc. in the field of electrical and electronic engineering, from Lahijan Azad University in

Dr. Shahram Mohanna received a Ph.D. degree in electronics engineering from the University of Manchester in July 2006. He worked as a research assistant in Sensing, Imaging and Signal Processing (SISP) Research Centre at the University of Manchester from 2002 to 2006. During 2012 and 2016, he joined the University of Nottingham Malaysia (UNM) as an associate professor until September 2016

Dr. Amir Nader Askarpour received the B.S. degree in electrical engineering from the Sharif University of Technology, Tehran, Iran, in 2004, and the M.S. and Ph.D. degrees in electrical engineering from the University of Tehran, Tehran, in 2006 and 2012, respectively. He was a post-doctoral researcher with the University of Texas, Austin, TX, USA, from 2012 to 2014. He is currently an assistant professor with the Amirkabir University of Technology (Tehran Polytechnic), Tehran, and also a member of the Microwave/MM-Wave and Wireless Communication Research Laboratory. He delivered several articles in international conferences and has published 17 papers in indexed journals.